A NOVEL IMAGING APPROACH FOR HIGH RESOLUTION SQUINTED SPOTLIGHT SAR BASED ON THE DERAMPING-BASED TECHNIQUE AND AZIMUTH NLCS PRINCIPLE

D.-X. An[*], Z.-M. Zhou, X.-T. Huang, and T. Jin

School of Electronic Science and Engineering, National University of Defense Technology, Changsha, Hunan 410073, P. R. China

Abstract—The imaging problem of spotlight synthetic aperture radar (SAR) in the presence of azimuth spectrum folding phenomenon can be resolved by adopting the azimuth deramping-based technique and traditional stripmap SAR imaging algorithm, and this method is the so-called two-step processing approach. However, when the spotlight SAR operates on squinted mode, the echo two-dimensional (2D) spectrum is shifted and skewed due to the squint angle. In such case, the original two-step processing approach is not suitable anymore. This paper presents a novel imaging algorithm using the deramping-based technique and azimuth nonlinear chirp scaling (ANLCS) technique. First, the problem of azimuth spectrum folding phenomenon in squinted spotlight SAR is analyzed. Subsequently, based on the analysis results, the linear range walk correction (LRWC) is applied for removing the squint angle impacts on signal azimuth coarse focusing. At last, a modified azimuth NLCS algorithm is proposed for overcoming the depth of focus (DOF) limitation problem that induced by the LRWC preprocessing. Point targets simulation results are presented to validate the effectiveness of the proposed algorithm to process squinted spotlight SAR data with azimuth spectrum folding phenomenon.

1. INTRODUCTION

Spotlight synthetic aperture radar (SAR) [1–8] offers finer azimuth resolution than that achieved in stripmap SAR, because its antenna is steered to illuminate the same scene centre for a loner period.

This imaging mode results in higher Doppler bandwidth signals for a high resolution in azimuth than that in stripmap SAR. However, the elaborate steering of the antenna results in an adverse phenomenon that the total azimuth signal bandwidth might span over several pulse repetition frequency (PRF) intervals, i.e., the so-called azimuth spectral folding phenomenon [5, 6]. This phenomenon limits the straightforward application of traditional stripmap SAR imaging algorithm. Although the polar format algorithm (PFA) [1, 2] can resolve this problem, its application is limited due to its complex and low-efficiency two-dimensional (2D) nonuniform interpolation operation. In past years, three class approaches have been developed to overcome the azimuth spectral folding and extended the focusing capability of traditional stripmap imaging algorithm for the spotlight SAR imaging. They are subapertures, azimuth upsampling, and azimuth deramping-based technique, respectively. The application of subapertures is limited due to its complex implementation and relative low-efficiency, which are induced by the necessary overlap between subapertures and complicated recombination. As for the upsampling approach, large zero padding increases the whole imaging computation load. Compared to aforementioned two algorithms, the azimuth deramping-based approach is more efficient and simpler.

The existing azimuth deramping-based approach [5–7] are derived based on the broadside spotlight SAR signal model, where the pointing direction of the antenna beam is perpendicular to the flight path at the azimuth center time. However, besides the broadside spotlight SAR, the squinted SAR is another important working mode, where there is an offset angle between the pointing direction of the antenna and the zero Doppler plane at azimuth center time. Compared with broadside mode, the squint mode can increase the flexibility of SAR system, provide information about surface structure through the measurement of the azimuth angle dependence of backscatter and enlarge the extension of azimuth focused scene within a single image. Thus, the investigation on squinted spotlight SAR imaging is especially significant. To extend the traditional deramping-based approach for the squinted spotlight SAR imaging, a modified deramping-based approach with Doppler controid correction using the azimuth linear phase term correction is proposed in [5]. However, from the analysis carried out in this paper, we can find that the azimuth linear phase term correction just partially removes the impacts of squint angle on signal azimuth coarse focusing. Using the modified two-step processing approach with integrated the azimuth linear phase term correction, only the targets at the scene center can be well focused, while the targets at the scene azimuth edge are still defocused and some "ghost

targets" are generated due to the residual folded spectrum, and the focused quality of the integrated image is dissatisfactory.

In this paper, a novel imaging algorithm is proposed based on the deramping-based technique and the azimuth nonlinear chirp scaling (ANLCS) technique [9, 10]. The proposed algorithm combines the advantages of the efficient azimuth deramping-based technique and ANLCS technique. First, by exactly analyzing the characteristics of the spectral folding phenomenon of the squinted spotlight SAR, the linear range walk correction (LRWC) is applied as a preprocessing step for the Doppler centroid correction. After the preprocessing step, the impact of squint angle on azimuth coarse focusing is completely removed, and the correct 2D spectrum is obtained. Then, the azimuth deramping-based technique is applied to overcome the azimuth spectral folding problem. At last, a modified ANLCS algorithm is applied for resolving the depth of focus (DOF) problem, which is arising from the LRWC.

This paper is organized as follows. Section 2 analyzes the azimuth spectral folding problem of squint spotlight SAR data, and the LRWC preprocessing is introduced for removing the squint angle impacts and the significant range walk affect. By this preprocessing, the traditional deramping-based azimuth coarse focusing for squinted spotlight SAR is derived in Section 3. Subsequently, Section 4 derives the precise focusing of the azimuth coarse focused signal. In this section, to obtain the high focused quality of high resolution large scene squinted SAR data, a modified ANLCS algorithm is proposed and derived in detailed. Section 5 shows that whole signal processing flowchart of the proposed algorithm, and simulation experiments are carried out in Section 6 to prove the effectiveness of proposed algorithm. Finally, Conclusions are summarized in Section 7.

2. PROBLEM STATEMENT

2.1. Squinted Spotlight SAR Signal Model

Figure 1 shows the geometry of squinted spotlight SAR in the slant range plane. The SAR sensor travels along the azimuth direction, which is parallel to the X-axis. The platform position at azimuth time zero is at point O, which is also the synthetic aperture center. The squint direction is defined as the direction from the synthetic aperture center to the imaging scene center. $(x_c, r_{s0} \cos \theta_s)$ is the observed scene center, where r_{s0} is the distance between the synthetic aperture center and the illuminated spot scene center, and θ_s is the squint angle, which is defined as the angle between the range direction and the squint direction. Furthermore, r_0 is the slant range between target P and the
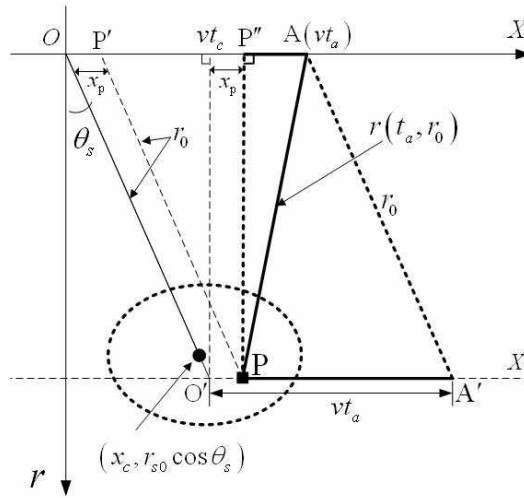
Figure 1. Acquisition geometry of squint spotlight SAR in the slant-range plane.

platform trajectory along the squint direction, i.e., $r_0 = \overline{PP'}$, and the instant slant range at time t_a is $r(t_a; r_0)$. $x_p = vt_p \in [-X_s/2, X_s/2]$ is the distance between the synthetic aperture center O and point P', and X_s is the illuminated spot area at range r_0. X' is the line passing through target P and parallel to the X-axis, while lines OO', PP', and AA' are parallel to each other. Here, note that we also have assumed the platform trajectory to be a straight line, as that described in [5], and all the derivations and simulations presented in this paper are all carried out based on this precondition.

Using the relationship of triangle APA', we can obtain the expression of instantaneous range $r(t_a; r_0)$ and its Taylor expansion, which is given by

$$r(t_a; r_0) = \sqrt{(vt_a - vt_p)^2 + r_0^2 - 2r_0(vt_a - vt_p)\sin\theta_s}$$

$$\approx r_0 - \frac{\lambda_c}{2}f_{dc}(t_a - t_p) - \frac{\lambda_c}{4}f_{dr}(t_a - t_p)^2 + \ldots \quad (1)$$

where $x_a = vt_a$ denotes the instant azimuth position of the platform. The last row of (1) shows that the instant range can be formulated by its Doppler centroid f_{dc} and Doppler rate f_{dr} [11], where $f_{dc} = 2v\sin\theta_s/\lambda_c$ and $f_{dr} = -\frac{2v^2\cos^2\theta_s}{\lambda_c r_0}$. The variable $\lambda_c = c/f_c$ is the center wavelength, where c and f_c denote the speed of light and the center frequency, respectively.

Let us assume a Linear Frequency Modulation (LFM) [12] pulse

with duration time T_p transmitted by the radar, which is denoted as

$$ss(\tau, t_a; r_0) = a_r \left[\frac{\tau}{T_p}\right] a_a \left[\frac{t_a}{T_{\text{spot}}}\right] \exp\left(j2\pi f_c \tau + j\pi\gamma\tau^2\right) \qquad (2)$$

where τ is the fast time, γ is the chirp rate, and T_{spot} is the full synthetic aperture time. $a_r \sim \text{rect}[\cdot]$ denotes the envelope of the transmitted range pulse and $a_a \sim \text{rect}[\cdot]$ denotes the two way azimuth antenna pattern. The expression of the echo signal in the range frequency and azimuth time domain is given by

$$Ss(f_r, t_a; r_0) \approx A_r(f_r) a_a \left[\frac{t_a}{T_{\text{spot}}}\right] \exp\left(j\pi\frac{f_r^2}{\gamma}\right) \exp\left[-j\frac{4\pi(f_r+f_c)}{c}r(t_a; r_0)\right] \quad (3)$$

where f_r is the range frequency and $A_r(f_r)$ is the amplitude of the range frequency signal. In the following sections, a description of the proposed method based on the above-mentioned equations is detailed.

2.2. Squint Angle Impact on Azimuth Coarse Focusing

In spotlight SAR, the Doppler centroid of the 2D spectrum is given by

$$f_{dc}(f_r) = \frac{2f_c v \cos^2\theta_s}{cr_0}x_p + \frac{2f_c \sin\theta_s}{c} + \frac{2f_r \sin\theta_s}{c} \qquad (4)$$

In the right side of (4), there are three terms. The first term is related to the target azimuth position x_p, which causes an azimuth-dependent shift of the 2D spectrum. The second term is related to the squint angle θ_s, which causes an azimuth-independent shift of the 2D spectrum. The third term is a linear function of the range frequency f_r, which causes a skew phenomenon of the 2D spectrum. From (4), we can find that, compared to the squinted stripmap SAR, the 2D spectrum of the squinted spotlight SAR has an extra azimuth-dependent shift. So, the target farthest apart from the azimuth reference position has the largest azimuth-dependent shift.

The basis of azimuth coarse focusing is to reduce the signal azimuth bandwidth by changing the chirp rate of azimuth signal, and allows achieving a bulk data compression and pixel spacing smaller than the expected azimuth resolution of the final image. However, in the traditional azimuth coarse focusing, the Doppler centroid of the spectrum is unchanged.

For simplicity and without loss of generality, let us neglect the Doppler ambiguity problem, and just consider the variation of the baseband Doppler centroid [1, 13] in the azimuth coarse focusing. In the 2D spectrum, the folded part of the baseband Doppler centroid is folded in unit of F_a. However, after performing the
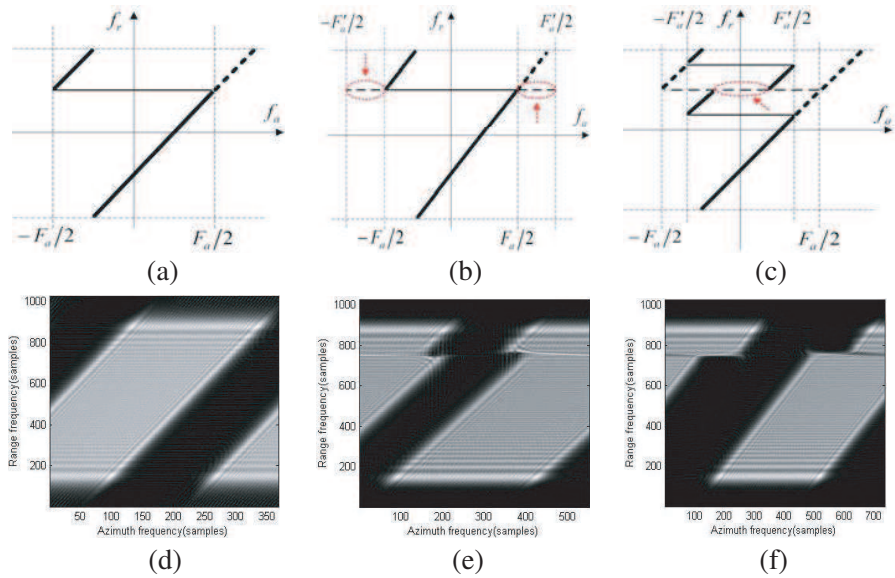
(a)   (b)   (c)

(d)   (e)   (f)

Figure 2. Illustration of the variation of the 2D spectrum. (a) Original Doppler centroid. (b) After coarse focusing $(F_a' \geq F_a)$. (c) After coarse focusing $(F_a' < F_a)$. (d) Original 2D spectrum. (e) After coarse focusing $(F_a' \geq F_a)$. (f) After coarse focusing $(F_a' < F_a)$.

azimuth coarse focusing, the azimuth signal will be sampled by a new sampling frequency, which is imposed by the choice of the deramping function modulation rate. Let F_a' denote the new azimuth sampling frequency [5, 6]. Therefore, in the coarse focused signal, the baseband Doppler centroid will be folded again, but in unit of F_a'. In the case of $F_a \neq F_a'$, the change in the sampling frequency causes a discontinuity (pointed by the arrow) in the 2D spectrum of the coarse focused signal, as shown in Figures 2(a)∼(c). The bold solid lines denote the Doppler centroid lying in (or folded into) the $[-F_a/2, +F_a/2]$ range, while the bold dashed lines denote the original parts of the Doppler centroid before folding. Corresponding to Figures 2(a)∼(c), Figures 2(d)∼(f) gives the 2D spectrum of a simulated target before and after performing the azimuth coarse focusing.

From above analysis, we can observe that the discontinuity in the 2D spectrum of the coarse focused signal is caused by two factors, namely, the Doppler centroid wrapping of the raw signal and the change in the azimuth sampling frequency in the azimuth coarse focusing. When these two conditions are simultaneously satisfied, a discontinuity distortion in the 2D spectrum of the coarse focused signal occurs. For the broadside spotlight SAR, the 2D spectrum is

not skewed and the Doppler centroid induced by the squint angle is equal to zero. In such a case, there is no Doppler centroid wrapping in the 2D frequency domain, and the azimuth coarse focusing can be directly applied on the raw signal. However, for the squinted spotlight SAR, in the raw signal, there is always a certain degree of folding of the Doppler centroid as a result of the PRF constraints and the skewing of the 2D spectrum as well as the nonzero Doppler shift. The discontinuity of the 2D spectrum of the coarse focused signal not only deteriorates the focused quality, but also generates "ghost targets" in the final SAR image. Therefore, to obtain the correct coarse focused signal, a preprocessing operation to remove the impacts of the Doppler centroid wrapping should be applied prior to the implementation of the azimuth coarse focusing.

3. AZIMUTH COARSE FOCUSING

3.1. Doppler Centroid Correction Preprocessing

To remove the impacts of squint angle on azimuth coarse focusing, an azimuth linear phase term $\exp(-j4\pi f_c \sin\theta_s t_a/c)$ is multiplied with the echo signal [5]. For the simplicity of description, we called this method as the azimuth linear phase correction (ALPC). According to (4), we can find that the function of the ALPC is to compensate the Doppler centroid caused by the squint angle (Corresponding to the second term in (4)), and the 2D spectrum will be shift $-2f_c \sin\theta_s/c$ in the azimuth direction. After applying the ALPC operation, target 2D spectrum center (Corresponding to the first term in (4)) will be dependent on its azimuth position. And the linear relationship between the Doppler centroid and range frequency is unchanged (See the third term in (4)), so the skew phenomenon of 2D spectrums still exist.

Figure 3 illustrates the echo signal preprocessing by different methods. In Figure 3(a), line ① and line ② denote the Doppler centroids of the point targets, which are located at the azimuth scene center and at the azimuth border, respectively. As shown in Figure 3(b), after applying the ALPC operation, the wrap around of the Doppler centroid corresponding to line ① disappears. However, for the Doppler centroid of line ②, a residual wrap around phenomenon still exists, which will has influence on the azimuth coarse focusing. Accordingly, this method cannot completely remove the impact of the folded Doppler centroid on the azimuth coarse focusing.

From the above-mentioned analysis, we can observe that if we want to completely solve the Doppler centroid wrap around problem, the skewing of the 2D spectrum must be corrected besides avoiding the azimuth shift of the 2D spectrum. Based on this idea, the linear range
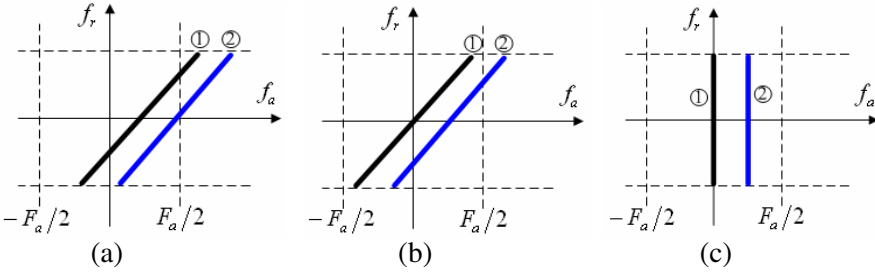
Figure 3. Illumination of Doppler centroid correction preprocessing. (a) Original Doppler centroid. (b) After applying the ALPC. (c) After applying the LRWC.

walk correction (LRWC) [11] is used in this paper. The correction phase term is given by

$$C(f_r, t_a) = \exp\left[-j\frac{4\pi f_c}{c}v\sin\theta_s t_a\right]\exp\left[-j\frac{4\pi f_r}{c}v\sin\theta_s t_a\right] \quad (5)$$

From (5), we can note that the function of the linear range walk correction includes two aspects: First, removing the Doppler shift induced by the squint angle (Corresponding to the first exponential term in (5)); and second, correcting skewing of the 2D spectrum (Corresponding to the second exponential term in (5)).

Figure 3(c) shows the 2D spectrum after applying the LRWC operation. It is evident that the wrap around phenomenon of the Doppler centroid of all the targets has been removed. Besides, by correcting the skewing of the 2D spectrum, the significant range walk effect in the RCM is also greatly mitigated, which simplifies the following SAR imaging processing.

On multiplying (5) with (3), yields

$$\begin{aligned}
Ss'(f_r, t_a; r_0) &= W_r(f_r)w_a\left[\frac{t_a}{T_{\text{spot}}}\right]\exp\left(-j\pi\frac{f_r^2}{\gamma}\right) \\
&\quad \exp\left[-j\frac{4\pi(f_r + f_c)}{c}(r(t_a; r_0) + v\sin\theta_s t_a)\right] \quad (6)
\end{aligned}$$

3.2. Azimuth Coarse Focusing Based on Deramping Technique

Let $s_{ref}(t_a; r_{ref})$ denote the azimuth coarse focusing reference signal

$$s_{ref}(t_a; r_{ref}) = \exp\left(-j\pi f_{dr,ref}t_a^2\right) \quad (7)$$

where r_{ref} is the selected reference range, $f_{dr,ref} = -\frac{2v^2\cos^2\theta_s}{\lambda_c r_{ref}}$ is the Doppler chirp rate of the reference azimuth signal. Let $ss''(t_a; r_0)$

denote the azimuth coarse focused signal, and the azimuth coarse focusing processing can be expressed as

$$ss''(t_a; r_0) = ss'(t_a; r_0) \otimes_{az} s_{ref}(t_a; r_{ref}) \tag{8}$$

where symbol $\otimes_{az}$ denotes the azimuth convolution. After this application, the targets at the reference ranges are correctly focused in azimuth direction, but the targets at other ranges are only partially focused. It is necessary to focus the partially focused targets in a subsequent operation in order to obtain precise focusing over the whole scene.

4. PRECISE FOCUSING

4.1. Range Focusing

By applying the two-dimensional Fourier transform of (8), the signal spectrum can be obtained

$$SS''(f_r, f_a; r_0) = SS'(f_r, f_a; r_0) \cdot \exp\left[-j\pi\left(f_a^2/f_{dr,ref}\right)\right] \tag{9}$$

where $SS'(f_r, t_a; r_0)$ is the spectrum of azimuth preprocessed signal, and the exponential term is the spectrum of azimuth reference signal. To obtain the azimuth preprocessed signal spectrum, rewriting (1) as follows

$$r(t_a; r_0) \approx \sqrt{r_0^2 + v^2 \cos^2\theta_s(t_a - t_p)^2} - v(t_a - t_p)\sin\theta_s$$
$$+ \frac{v^3 \sin\theta_s \cos^2\theta_s}{2r_0}(t_a - t_p)^3 \tag{10}$$

In (10), only the odd-order components of the higher order Taylor ($\geq$ 5th) expansion terms are ignored. This approximation has a very high accuracy.

Substituting (10) into (6), and applying the azimuth FFT, yields

$$SS'(f_r, f_a; r_0) \approx W_r(f_r)W_a(f_a)$$
$$\exp\left[-j\frac{4\pi(f_r+f_c)}{c}vt_p\sin\theta_s\right]\exp(-j2\pi f_a t_p)\exp\left(-j\pi\frac{f_r^2}{\gamma}\right)$$
$$\times \exp\left[-j\frac{4\pi r_0}{c}\sqrt{(f_r + f_c)^2 - \left(\frac{cf_a}{2v\cos\theta_s}\right)^2}\right]$$
$$\exp\left[jr_0\frac{2\pi sin\theta_s f_a^3}{\lambda_c \cos\theta_s(f_{aM}^2 - f_a^2)^{3/2}}\right] \tag{11}$$

where $f_{aM} = 2v\cos\theta_s/\lambda_c$. For the cross-coupling phase compensation, there are several options could be chosen, such as the range-Doppler

method [1], chirp scaling [13] and Stolt interpolation [13, 14]. Here, we use the modified Stolt interpolation [15] due to its simpler derivation. According to the cross-coupling term in (11), the following modified Stolt variable mapping is applied

$$f_r' = \sqrt{(f_r + f_c)^2 - \left(\frac{cf_a}{2v\cos\theta_s}\right)^2} - \sqrt{f_c^2 - \left(\frac{cf_a}{2v\cos\theta_s}\right)^2} \quad (12)$$

where f_r' is the mapped range frequency to be compared with f_r. Applying azimuth FFT on the signal after the Stolt interpolation, yields

$$sS''(\tau, f_a; r_0) = \mathrm{sinc}\left[B_r\left(\tau - \frac{2(r_0 + vt_p\sin\theta_s)}{c}\right)\right] W_a(f_a)\exp(-j2\pi f_a t_p)$$

$$\times \exp\left[-j\frac{4\pi r_0}{c}\sqrt{f_c^2 - \left(\frac{cf_a}{2v\cos\theta_s}\right)^2}\right.$$

$$\left. + jr_0\frac{2\pi\sin\theta_s}{\lambda\cos\theta_s}\frac{f_a^3}{(f_{aM}^2 - f_a^2)^{3/2}}\right] \quad (13)$$

where B_r is signal bandwidth. Inspecting (13), we can find that the LRWC results in an azimuth-dependent displacement in the range envelope. In other words, the targets that have different initial slant ranges now may lie in the same range. This is the so-called DOF problem [11], which will hamper the direct use of the traditional azimuth filtering processing, and make the azimuth compression more complicated.

4.2. Azimuth Focusing

Let $\Psi(f_a; r_0)$ denote the phase of the range-focused signal (13), and rewrite it as

$$\Psi(f_a; r_0) = -2\pi t_p f_a - \frac{4\pi r_0}{\lambda_c}\left[1 - \left(\frac{f_a}{f_{aM}}\right)^2\right]^{1/2}$$

$$+ \frac{2\pi r_0\sin\theta_s}{\lambda_c\cos\theta_s}\frac{f_a^3}{f_{aM}^3}\left[1 - \left(\frac{f_a}{f_{aM}}\right)^2\right]^{-3/2} \quad (14)$$

where $f_{aM} = 2v\cos\theta_s/\lambda_c$. Under the assumption of $|f_a| \ll |f_{aM}|$, expanding (14) into a power series in f_a, yields

$$\Psi(f_a; r_0) \approx \psi_0 + \psi_1 f_a + \psi_2 f_a^2 + \psi_3 f_a^3 + \sum_{n=4}^{\infty} \psi_n f_a^n \quad (15)$$

The coefficients ψ_0, ψ_1, ψ_2, ψ_3 and ψ_n are given by

$$
\begin{cases}
\psi_0 = -\frac{4\pi r_0}{\lambda_c}; & \psi_1 = -\frac{2\pi x_p}{v} \\
\psi_2 = \frac{2\pi r_0}{\lambda_c f_{aM}^2} = -\frac{\pi}{K_a}; & \psi_3 = \frac{2\pi r_0 \sin\theta_s}{\lambda_c f_{aM}^3 \cos\theta_s} \\
\psi_n = \frac{1}{n!} \frac{\partial^n \Psi(f_a; r_0)}{\partial f_a^n}
\end{cases}
\tag{16}
$$

where $K_a = -\frac{2v^2 \cos^2\theta_s}{\lambda_c r_0}$ is the azimuth FM rate at range r_0. For the simplicity of description, we called the summation of the terms above the third-order as higher-order phase (HOP). Based on (15), let us carry out an analysis on the impacts of the azimuth mismatched filtering that induced by the LRWC preprocessing operation.

4.2.1. Depth of Focus Problem

The DOF problem is induced by the mismatch filtering of the second-order azimuth phase, i.e., the third expansion term in (15). For a specified SAR system, we can compute the range depth of focus (RDOF) δr_{RDOF} [11] as follows

$$
\delta r_{\text{RDOF}} = |x_p \sin\theta_s| \leq \frac{\rho_a^2 \cos^2\theta_s}{\lambda_c}
\tag{17}
$$

where ρ_a is the azimuth resolution. Using inequality (17), the corresponding azimuth depth of focus (ADOF) δx_{ADOF} can be computed as

$$
\delta x_{\text{ADOF}} = \frac{2\rho_a^2 \cos^2\theta_s}{\lambda_c |\sin\theta_s|}
\tag{18}
$$

From (17) and (18), we can find that δx_{ADOF} becomes smaller when azimuth resolution gets finer, squint angle gets larger, and/or wavelength gets longer. As an example, assuming an X-band squint SAR system with the following typical parameters: $\lambda_c = 0.03\,\text{m}$, $r_0 = 500\,\text{km}$, and $v = 7\,\text{km/s}$. Then, Figure 4 shows the relationship between δx_{ADOF} and the squint angle for typical azimuth resolution (ρ_a). From Figure 4, we can find that as the squint angle larger or the resolution higher, the ADOF decreases quickly. For example, with 1m resolution, the ADOF value is 344.2 m and 71.92 m at the squint angle of 30° and 50°, respectively. These ADOF values are far smaller than the illuminated scene size of the general spaceborne SAR system.

Due to the impacts of ADOF, different methods could be used for target azimuth focusing correspondingly with different real conditions. First, when the scene azimuth size is smaller than δx_{ADOF}, the impacts of ADOF limitation can be ignored, and the traditional matched filtering method can be directly applied for azimuth focusing. Second,
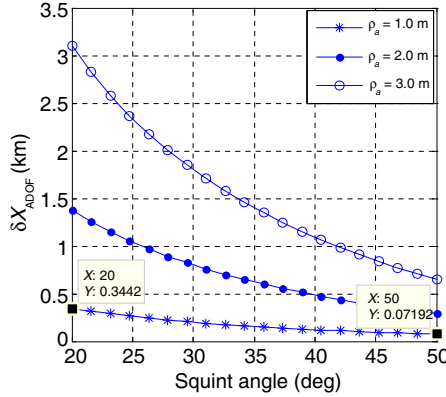
Figure 4. The relationship between ADOF and squint angle.

when the scene azimuth size is larger than δx_{ADOF}, the impacts of the ADOF limitation can not be ignored anymore, and a modified azimuth compression method is needed to obtain the well focused integrated SAR image. Obviously, the former case is simpler, while the latter case is more complicated and difficult.

4.2.2. Impacts of the Higher-order Phases

Besides the ADOF problem, the impacts of the higher-order ($\geq$ 3rd) phases mismatched filtering also need to be considered in the high resolution squinted SAR imaging.

Substituting $r_{\mathrm{LRWC}} = r_0 + x_p \sin \theta_s$ into the coefficient ψ_3, and we have

$$\psi_3 = \frac{2\pi \sin \theta_s}{\lambda_c f_{aM}^3 \cos \theta_s} (r_{\mathrm{LRWC}} - x_p \sin \theta_s) = \psi_{3,\,\mathrm{LRWC}} + \psi_{3,\,s} \cdot t_p \quad (19)$$

where $\psi_{3,\,\mathrm{LRWC}}$ and $\psi_{3,\,s}$ denote the azimuth-independent coefficient and the azimuth-dependent coefficient of the third-order phase, respectively. And their expressions are given by

$$\begin{cases} \psi_{3,\,\mathrm{LRWC}} = \frac{2\pi \sin \theta_s}{\lambda_c f_{aM}^3 \cos \theta_s} r_{\mathrm{LRWC}} \\ \psi_{3,\,s} = -\frac{2\pi v \sin^2 \theta_s}{\lambda_c f_{aM}^3 \cos \theta_s} \end{cases} \quad (20)$$

The maximum values of the azimuth-independent third-order phase (AITOP) and azimuth-dependent third-order phase (ADTOP) can be expressed as

$$\begin{cases} \phi_{\mathrm{AITOP}} = \psi_{3,\,\mathrm{LRWC}} \cdot f_{a,\max}^3 \big|_{f_{a,\max}=v/2\rho_a} \\ \phi_{\mathrm{ADTOP}} = \psi_{3,\,s} \cdot f_{a,\max}^3 \big|_{f_{a,\max}=v/2\rho_a} \end{cases} \quad (21)$$

Similarly, substituting $r_{\text{LRWC}} = r_0 + x_p \sin\theta_s$ into the coefficients ψ_n ($n \geq 4$) of the higher-order phases, yields

$$\psi_n = \frac{1}{n!}\frac{\partial^n \Psi(f_a; r_{\text{LRWC}})}{\partial f_a^n} + \frac{1}{n!}\frac{\partial^n \Psi(f_a; -x_p \sin\theta_s)}{\partial f_a^n}$$
$$= \psi_{n,LRWC} + \psi_{n,s} \cdot t_p \qquad (22)$$

where $\psi_{n,\text{LRWC}} = \frac{\psi_n}{r_0} r_{\text{LRWC}}$, $\psi_{n,s} = -\frac{\psi_n}{r_0} v \sin\theta_s$ denote the azimuth-independent coefficient and the azimuth-dependent coefficient of the nth-order phase, respectively. And the maximum values of the azimuth-independent HOP (AIHOP) and azimuth-dependent HOP (ADHOP) are given by

$$\begin{cases} \phi_{\text{AIHOP}} = \sum\limits_{n=4}^{\infty} \psi_{n,\text{LRWC}} \cdot f_{a,\max}^n|_{f_{a,\max}=v/2\rho_a} \\ \phi_{\text{ADHOP}} = \sum\limits_{n=4}^{\infty} \psi_{n,s} \cdot f_{a,\max}^n|_{f_{a,\max}=v/2\rho_a} \end{cases} \qquad (23)$$

Based on above derivation, let us carry out an analysis on the impacts of the azimuth-independent and azimuth-dependent phases. Assuming an X-band squinted SAR system with the following typical parameters: $\lambda_c = 0.03\,\text{m}$, $r_0 = 500\,\text{km}$, $v = 7\,\text{km/s}$. Figure 5 shows the AITOP and AIHOP versus squint angle for specific azimuth resolutions. From Figure 5, we can find that the azimuth independent phases gets larger when the squint angle gets bigger, and/or the azimuth resolution gets finer. Moreover, for the same configuration, the value of AITOP is much larger than that of AIHOP. In general SAR
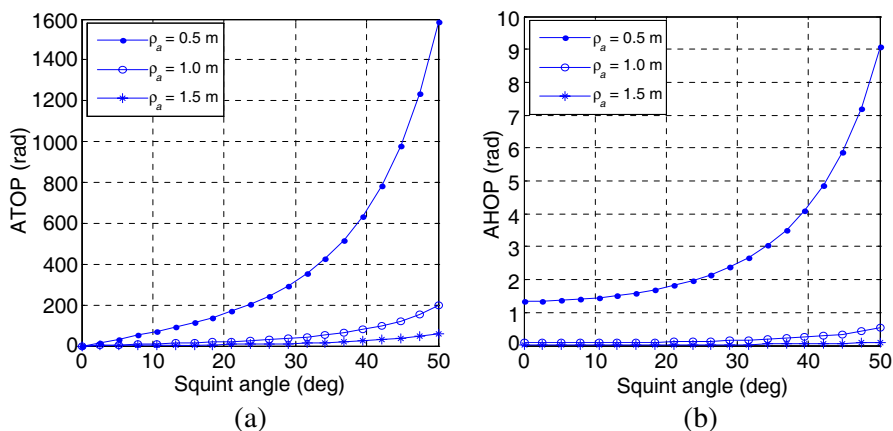

Figure 5. Azimuth-independent phases versus squint angle for specific azimuth resolutions. (a) AITOP, and (b) AIHOP.
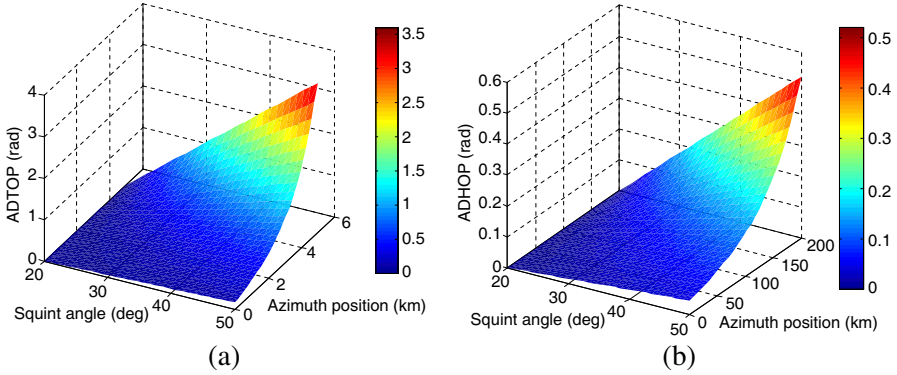
Figure 6. Azimuth-dependent phases versus squint angle and azimuth position. (a) ADTOP, and (b) ADHOP.

imaging, the impacts of the azimuth-independent phase can be ignored when they are smaller than the acceptable level $\pi/4$. Otherwise, their impacts must be considered, and the compensation method for removing the impacts should be performed.

Using the same simulation parameters, Figure 6 shows the azimuth-dependent third-order phase (ADTOP) and the azimuth-dependent higher-order phase (ADHOP) versus to squint angle and azimuth position for azimuth resolution of 1m. From Figure 6, we can find that the values of ADTOP and ADHOP are very small for most squinted SAR systems, but their values gets larger as the squint angle gets bigger, the resolution gets finer, and/or the azimuth position gets larger. When they are smaller than the acceptable level $\pi/4$, it is reasonable to ignore their impacts. Moreover, observing Figure 6(b), we can find that the ADHOP is smaller than $\pi/4$ in a very large scene. So, in most large scene high resolution squinted SAR imaging, it is reasonable to neglect the impacts of ADHOP. Compared to the ADHOP, the ADTOP has much larger value for the same azimuth position, so its impacts must be considered in the large scene high resolution squinted SAR imaging.

Based on above analysis, we neglect the ADHOP in the following derivation, and rewriting (13) as follows

$$sS''(\tau, f_a; r_{\text{LRWC}}) = \text{sinc}\left[B_r\left(\tau - \frac{2r_{\text{LRWC}}}{c}\right)\right]W_a(f_a)$$
$$\exp\left[-j\frac{4\pi(r_{\text{LRWC}} - vt_p\sin\theta_s)}{\lambda_c}\right]$$

$$\times \exp\left[j\psi_1 f_a - j\pi\frac{f_a^2}{K_a} + j(\psi_{3,\mathrm{LRWC}} + \psi_{3,s} \cdot t_p)f_a^3\right.$$

$$\left. +j\sum_{n=4}^{\infty}\psi_{n,\mathrm{LRWC}}f_a^n\right], \quad n = 4,\ldots,\infty \qquad (24)$$

The first exponential term is a constant, which has no impacts on the target focused quality and is ignored.

4.2.3. Azimuth Compression with the Modified ANLCS

Now, let us carry out a deep evaluation on the azimuth-dependent characteristic of the azimuth FM rate. To model the azimuth dependence of the FM rate, substituting $r_{\mathrm{LRWC}} = r_0 + vt_p\sin\theta_s$ into K_a and expanding it in terms of t_p and keeping up to the first-order, yields

$$K_a \approx -\frac{2v^2\cos^2\theta_s}{\lambda r_{\mathrm{LRWC}}} - \frac{2v^2\cos^2\theta_s}{\lambda r_{ref}}\frac{v\sin\theta_s}{r_{ref}}t_p = K_{\mathrm{LRWC}} + K_s \cdot t_p \quad (25)$$

where K_{LRWC} and K_s are given by

$$K_{\mathrm{LRWC}} = -\frac{2v^2\cos^2\theta_s}{\lambda_c r_{\mathrm{LRWC}}}, \quad K_s = \frac{v\sin\theta_s}{r_{\mathrm{LRWC}}} \qquad (26)$$

From (25), it is easy to find that the azimuth-dependent characteristic of the azimuth FM rate is very similar to the range-dependent characteristic of the range FM rate. Therefore, we can apply the chirp scaling principle used in the nonlinear chirp scaling (NCS) algorithm [16] to the azimuth signal for equalizing the azimuth FM rate, and this method is the so-called azimuth nonlinear chirp scaling (ANLCS) algorithm [8].

Based on above analysis, we just consider the impacts of ADTOP and ignore the impacts of ADHOP in the following derivation. The AITOP and AIHOP can be compensated by multiplying (24) with a function which is formulated as

$$H_{\mathrm{APC}}(f_a; r_{\mathrm{LRWC}}) = \exp\left[-j\psi_{3,\mathrm{LRWC}}f_a^3 - j\sum_{n=4}^{\infty}\psi_{n,\mathrm{LRWC}}f_a^n\right],$$

$$n = 4,\ldots,\infty \quad (27)$$

Multiplying (27) with (24), yields

$$sS''(\tau, f_a; r_{\mathrm{LRWC}}) = \mathrm{sinc}\left[B_r\left(\tau - \frac{2r_{\mathrm{LRWC}}}{c}\right)\right]W_a(f_a)$$

$$\exp\left[j\psi_1 f_a - j\pi\frac{f_a^2}{K_a} + j\psi_{3,s} \cdot t_p \cdot f_a^3\right] \quad (28)$$

Before performing the ANLCS operation, a fourth-order azimuth filter should be first applied, which is used for deriving the expressions for the chirp scaling phase function coefficients. The fourth-order filter factor is given by

$$H_{\mathrm{IF}}(f_a) = \exp\left[j\pi\left(Y_3 f_a^3 + Y_4 f_a^4\right)\right] \tag{29}$$

The azimuth filtering step is then represented by

$$sS''(\tau, f_a; r_{\mathrm{LRWC}}) = \mathrm{sinc}\left[B_r\left(\tau - \frac{2r_{\mathrm{LRWC}}}{c}\right)\right] W_a(f_a) \exp\left(j\psi_1 f_a\right)$$

$$\exp\left[-j\pi\frac{f_a^2}{K_a} + j\pi\left(Y_3 + \psi'_{3,s} t_p\right) f_a^3 + j\pi Y_4 f_a^4\right] \tag{30}$$

where $\psi'_{3,s} = \psi_{3,s}/\pi$. Transforming (30) into the azimuth time domain by the POSP, yields

$$ss''(\tau, t_a; r_{\mathrm{LRWC}})$$
$$= \mathrm{sinc}\left[B_r\left(\tau - \frac{2r_{\mathrm{LRWC}}}{c}\right)\right] w_a(t_a - t_p) \exp\left[j\pi K_a(t_a - t_p)^2\right]$$
$$\times \exp\left[j\pi(Y_3 + \psi'_{3,s} t_p) K_a^3 (t_a - t_p)^3\right] \exp\left[j\pi Y_4 K_a^4 (t_a - t_p)^4\right] \tag{31}$$

In above transformation, the cubic and quartic phases are assumed to be very small, and their impacts on the stationary point evaluation are ignored, i.e., the signal (30) is assumed to be dominantly linear FM, with the small nonlinear FM component. From (31), we can find that the expression of the azimuth modulation signal is similar to the range modulation, but they have quite different time scales.

After the azimuth filtering, a fourth-order chirp scaling factor is introduced for eliminating the azimuth dependence of the azimuth FM rate and compensating the AITOP. The fourth-order chirp scaling factor is given by

$$H_{\mathrm{ANLCS}}(t_a) = \exp\left(j\pi q_2 t_a^2 + j\pi q_3 t_a^3 + j\pi q_4 t_a^4\right) \tag{32}$$

Multiplying (31) with (32), yields

$$ss''(\tau, t_a; r_{\mathrm{LRWC}}) = \mathrm{sinc}\left[B_r\left(\tau - \frac{2r_{\mathrm{LRWC}}}{c}\right)\right] w_a(t_a - t_p)$$
$$\exp\left(j\pi q_2 t_a^2 + j\pi q_3 t_a^3 + j\pi q_4 t_a^4\right)$$
$$\times \exp\left[j\pi K_a(t_a - t_p)^2 + j\pi(Y_3 + \psi'_{3,s} t_p) K_a^3 (t_a - t_p)^3\right.$$
$$\left. + j\pi Y_4 K_a^4 (t_a - t_p)^4\right] \tag{33}$$

Transforming (33) into azimuth frequency by using the POSP again, yields

$$sS''(\tau, f_a; r_{\text{LRWC}})$$

$$= \text{sinc}\left[B_r\left(\tau - \frac{2r_{\text{LRWC}}}{c}\right)\right] W_a\left(\frac{f_a - q_2 t_p}{K_a + q_2}\right) \exp\left[-j2\pi \frac{f_a + K_a t_p}{K_a + q_2} f_a\right]$$

$$\times \exp\left\{j\frac{\pi}{(K_a + q_2)^2}\left[K_a(f_a - q_2 t_p)^2 + q_2(f_a + K_a t_p)^2\right]\right\}$$

$$\times \exp\left\{j\frac{\pi}{(K_a + q_2)^3}\left[(Y_3 + \psi'_{3,s} t_p)K_a^3(f_a - q_2 t_p)^3 + q_3(f_a + K_a t_p)^3\right]\right\}$$

$$\times \exp\left\{j\frac{\pi}{(K_a + q_2)^4}\left[Y_4 K_a^4(f_a - q_2 t_p)^4 + q_4(f_a + K_a t_p)^4\right]\right\} \quad (34)$$

Let $\Theta(f_a)$ denote the phase term of (34), and expressing it as a power series of t_p and f_a, yields

$$\begin{aligned}
\Theta(f_a) \approx\ & A\left(q_2, q_3, q_4, Y_3, Y_4, f_a, f_a^2, f_a^3, f_a^4\right) + B\left(q_2, q_3, q_4, Y_3, Y_4\right) t_p f_a \\
& + C\left(q_2, q_3, q_4, Y_3, Y_4\right) t_p^2 f_a + D\left(q_2, q_3, q_4, Y_3, Y_4\right) t_p f_a^2 \\
& + E\left(q_2, q_3, q_4, Y_3, Y_4\right) t_p^2 f_a^2 + F\left(q_2, q_3, q_4, Y_3, Y_4\right) t_p f_a^3 \\
& + G\left(q_2, q_3, q_4, Y_3, Y_4, t_p, t_p^2, t_p^3, t_p^4\right) \\
& + \phi_{res}\left(q_2, q_3, q_4, Y_3, Y_4, f_a, t_p\right) \quad (35)
\end{aligned}$$

There are seven terms in (35). The first term is due to the azimuth-independent phase modulation. The second term is target real azimuth position. The third term is the main factor that causes the geometric distortion of nonuniform shift in the azimuth direction. Because of the term t_p^2, the shift is always to the right, and the targets furthest away from the scene azimuth center suffer the most shift. In [8], an interpolation method is used for removing this geometric distortion and moves the focused target to the correct position. The fourth and the fifth terms as well as the sixth term are due to the azimuth-dependent phase modulation, which are the main factors that limit the size of the DOF. The seventh term is independent of the azimuth frequency, which has no impacts on target focused quality, and can be reasonably ignored if a magnitude image is the final product. But in the interferometric SAR, the impact of this term should be considered. The last term denotes the summation of all the other expansion series terms, which are very small and their impacts are neglected.

To eliminate the azimuth-dependent geometric distortion and the azimuth dependence of the azimuth filtering, we set the coefficient $B(q_2, q_3, q_4, Y_3, Y_4)$ to $-\pi/\alpha$, where $\alpha \neq 0.5$ is an introduced constant factor. And all the other coefficients of the terms, which contain $t_p^k f_a^l$,

$k \neq 0$, $l \neq 0$ in (35) are set to zero. Then we have five equations for five unknowns as

$$\begin{cases} B\left(q_2, q_3, q_4, Y_3, Y_4\right) = -\pi/\alpha \\ C\left(q_2, q_3, q_4, Y_3, Y_4\right) = 0 \\ D\left(q_2, q_3, q_4, Y_3, Y_4\right) = 0 \\ E\left(q_2, q_3, q_4, Y_3, Y_4\right) = 0 \\ F\left(q_2, q_3, q_4, Y_3, Y_4\right) = 0 \end{cases} \tag{36}$$

Solving (36), and the parameters are given by

$$\begin{cases} q_2 = K_{\mathrm{LRWC}}(2\alpha - 1) \\ q_3 = \frac{K_s(2\alpha - 1)}{3} \\ q_4 = \frac{K_s^2(8\alpha + 1) + 3\psi'_{3,s} K_{\mathrm{LRWC}}^4(2\alpha - 1)}{12 K_{\mathrm{LRWC}}} \\ Y_3 = \frac{K_s(4\alpha - 1)}{3 K_{\mathrm{LRWC}}^3 (2\alpha - 1)} \\ Y_4 = \frac{K_s^2(40\alpha^2 - 12\alpha - 1) + 3\psi'_{3,s} K_{\mathrm{LRWC}}^4(8\alpha^2 - 6\alpha + 1)}{12 K_{\mathrm{LRWC}}^5 (2\alpha - 1)^2} \end{cases} \tag{37}$$

Substituting (37) into (34), we can obtain the range-Doppler (range time and azimuth Doppler) domain echo signal after implementing the fourth-order nonlinear chirp scaling operation, which is given by

$$sS''(\tau, f_a; r_{\mathrm{LRWC}})$$
$$= \operatorname{sinc}\left[\tau - \frac{2r_{\mathrm{LRWC}}}{c}\right] W_a\left[\frac{f_a - q_2 t_p}{1/(K_{\mathrm{LRWC}} + q_2) - K_s t_p/(K_{\mathrm{LRWC}} + q_2)^2}\right]$$
$$\exp\left[-j2\pi \frac{t_p}{2\alpha} f_a\right] \times \exp\left[-j\pi \frac{1}{K_{\mathrm{LRWC}} + q_2} f_a^2 + j\pi \frac{Y_3 K_{\mathrm{LRWC}}^3 + q_3}{(K_{\mathrm{LRWC}} + q_2)^3} f_a^3\right.$$
$$\left. + j\pi \frac{Y_4 K_{\mathrm{LRWC}}^4 + q_4}{(K_{\mathrm{LRWC}} + q_2)^4} f_a^4\right] \tag{38}$$

Inspecting (38), it is evident that the azimuth-dependent characteristic of the azimuth modulation terms has been completely removed, and the azimuth-dependent geometric distortion is also corrected. From the envelope $W_a[\cdot]$ in (38), we can find that there is a shift in the azimuth spectrum. In most cases, this spectrum shift has no impacts on the imaging results because the azimuth signal is usually oversampled. Therefore, as long as the shift in the spectrum envelope stays within this constraint, no aliasing of the spectrum will occur. However, if the spectrum shift exceeds the constraint, the spectrum extension method should be applied to resolve the spectrum aliasing problem [17].

From (38), the azimuth compression factor is given by

$$H_{\mathrm{AC}}(f_a; r_{\mathrm{LRWC}}) = \exp\left[j\pi \frac{1}{K_{\mathrm{LRWC}} + q_2} f_a^2 - j\pi \frac{Y_3 K_{\mathrm{LRWC}}^3 + q_3}{(K_{\mathrm{LRWC}} + q_2)^3} f_a^3\right.$$
$$\left. - j\pi \frac{Y_4 K_{\mathrm{LRWC}}^4 + q_4}{(K_{\mathrm{LRWC}} + q_2)^4} f_a^4\right] \tag{39}$$

Multiplying (39) with (38), and transforming the result signal into the azimuth time domain, then the final focused SAR image is obtained

$$ss''(\tau, t_a; r_0)$$
$$= \mathrm{sinc}\left[\tau - \frac{2(r_0 + vt_p \sin\theta_s)}{c}\right] \mathrm{sinc}\left[t_a - \frac{t_p}{2\alpha}\right] \exp\left(j\frac{q_2 t_p}{K_a + q_2} t_a\right) \quad (40)$$

From (40), we can find that the target is focused at position $[r_0 + x_p \sin\theta_s, \frac{x_p}{2\alpha}]$, which is offset from the correct position. The method to resolve this problem is simple. First, multiplying the focused target signal with $\exp(-j2\pi x_p \sin\theta_s f_r)$ in the range frequency and azimuth time domain, and the displacement error in range direction can be eliminated. Second, adjusting the azimuth sampling interval Δx by multiplying with 2α puts the target at a position matching the real azimuth coordinates.

5. FLOWCHART OF THE PROPOSED APPROACH

Based on the derivations carried out in previous sections, Figure 7 shows the whole imaging flowchart of the proposed approach for processing the squinted spotlight SAR data in presence of the azimuth spectrum folding problem, and X_s is the azimuth size of the illuminated spot scene. The whole imaging processing consists of three steps: signal preprocessing, azimuth coarse focusing and precise focusing.
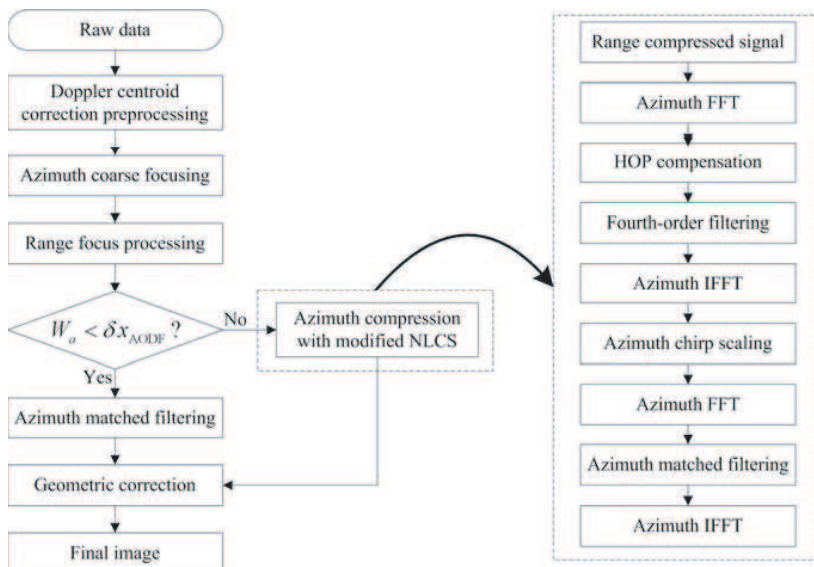

Figure 7. Signal processing flowchart of the proposed algorithm.

6. SIMULATION EXPERIMENTS

To prove the correctness of the theory analysis and the effectiveness of the proposed approach in this paper, targets imaging simulation experiments were carried out. The simulation parameters are shown in Table 1.

The simulation uses an array of 25 targets, which are shown in Figure 8. Target 13 is set in the scene center. All the targets are 1.5 km apart from one another in range direction, and 0.75 km apart from one another in azimuth direction. Using the simulated parameters shown in Table 1, we can calculate that the total azimuth bandwidth of the echo signal is about 9 kHz, which is much larger that the PRF, so the signal azimuth spectrum will be folded. Moreover, it is easy to compute that the ADOF δx_{ADOF} is about 344 m, which is much smaller than the size of the scene azimuth width, so the impacts of the ADOF must be considered in the imaging. To obtain a well focused quality of the integrated real image, the proposed algorithm with integrated the modified ANLCS is applied for the simulated data imaging.

Figure 9 shows the imaging results obtained by different methods. To clearly observe target focused quality, none weighting or sidelobe

Table 1. Simulation parameters.

Center frequency	Pulse bandwidth	Sampling frequency	Center range
10 GHz	150 MHz	180 MHz	500 km

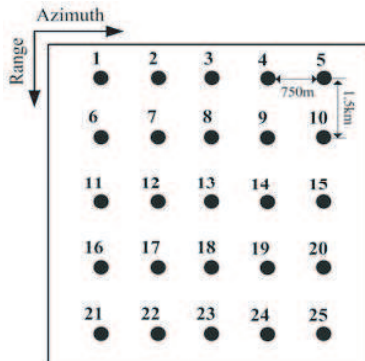| Azimuth resolution	PRF	Squint angle	Scene size (Range × azimuth)
1 m	4.5 kHz	20°	6 km × 3 km

Figure 8. Targets distribution.

suppressing measure are applied. Moreover, to observe all the "ghost targets" in the SAR image, a different extension region is kept in the image shown in Figure 9(a) in the range and azimuth directions. Figure 9(a) shows the result obtained by the two-step processing approach with integrated the ALPC [5]. Observing the image, we can find that the targets located around the scene azimuth center are well focused. However, for the targets at the azimuth border, due to the impacts of the residual wrap around the coarse focused data, their focused quality is still unsatisfactory and some "ghost targets" (Circled by the red dashed rectangle) could be observed. When compared with the above-mentioned result, the imaging result obtained by our proposed algorithm has better focused quality, as shown in Figure 9(b). It can be found that not only the "ghost targets" completely disappear, but also all the targets are well focused.
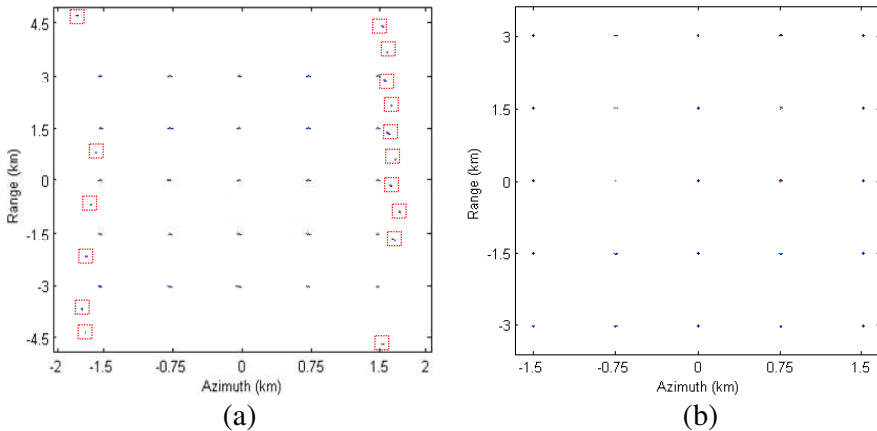

(a)   (b)

Figure 9. Simulation results by using (a) two-step processing approach with integrated ALPC operation, and (b) our proposed algorithm with integrated ANLCS operation.

Table 2. Imaging qualities analysis of point targets.

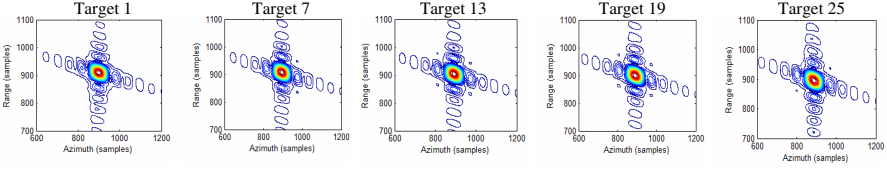|	Range			Azimuth		
	ρ_r (m)	PSLR (dB)	ISLR (dB)	ρ_a (m)	PSLR (dB)	ISLR (dB)
Target 1	0.89	-13.25	-10.98	0.87	-13.12	-10.54
Target 7	0.88	-13.22	-10.54	0.86	-13.19	-10.11
Target 13	0.87	-13.23	-10.48	0.86	-13.29	-10.35
Target 19	0.88	-13.28	-10.43	0.87	-13.11	-10.23
Target 25	0.89	-13.26	-10.73	0.86	-13.09	-10.62

Figure 10. The subimages extracted from Figure 9(b).
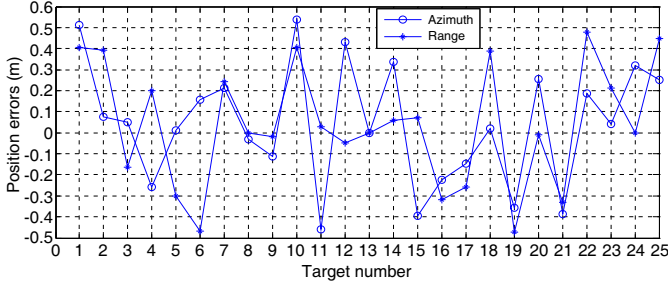

Figure 11. Illumination of the targets position errors.

In order to clearly observe the quality of the simulated targets by our proposed algorithm, we extract the subimages of targets 1, 7, 13, 19 and 25 from Figure 9(b), as shown in Figure 10. All the extracted subimages are interpolated by the same zeros padding the spectrum in the energy gaps and inverse transforming. Moreover, to clearly observe target focused quality, no weighting or sidelobe suppressing measure are applied. Observing the subimages shown in Figure 10, it is easy to find that all the targets are well focused, which means the AODF limitation problem is effectively resolved.

Moreover, Table 2 summarizes the measured resolutions ρ_a (3 dB width), the Peak Sidelobe Ratio (PSLR) and the Integrated Sidelobe Ratio (ISLR) [13] of the extracted targets in azimuth dimension, which could provide a quantitative evaluation on the targets focused quality. It can be observed that the focusing is nearly perfect for all the targets corresponding to the theoretical values.

Figure 11 shows the position errors of targets $1 \sim 25$ between their real positions and the theoretic positions. Observing Figure 11, it is easy to find that the position errors of all the targets in both range and azimuth direction are smaller than 0.5 resolution cell, which is so small and can be neglected in most cases.

7. CONCLUSIONS

In this paper, a novel imaging algorithm for large scene high resolution squinted spotlight SAR based on the deramping-based technique and

ANLCS principle is demonstrated. A deep analysis on the azimuth spectrum folding phenomenon of squinted spotlight SAR is carried out first and the reason of the squint angle impacts the azimuth coarse focusing is found out. Based on the analysis result, the LRWC preprocessing is applied for removing the squint angle impacts, and the correct azimuth coarse focusing result is obtained. At last, a modified ANLCS algorithm is proposed for resolving the DOF problem induced by the LRWC preprocessing, so the squinted spotlight SAR image with high focused quality is obtained. The signal processing flow of the proposed algorithm is derived in detailed, and the presented approach is validated by point targets simulation experiments.

ACKNOWLEDGMENT

REFERENCES

1. Carrara, W. G., R. S. Goodman, and R. M. Majewski, *Spotlight Synthetic Aperture Radar: Signal Processing Algorithms*, Artech House, Norwood, MA, 1995.

2. Sun, J., S. Mao, G. Wang, and W. Hong, "Polar format algorithm for spotlight bistatic SAR with arbitrary geometry configuration," *Progress In Electromagnetics Research*, Vol. 103, 323–338, 2010.

3. Guo, D., H. Xu, and J. Li, "Extended wavenumber domain algorithm for highly squinted sliding spotlight SAR data processing," *Progress In Electromagnetics Research*, Vol. 114, 17–32, 2011.

4. Koo, V. C., Y. K. Chan, V. Gobi, M. Y. Chua, C. H. Lim, C.-S. Lim, C. C. Thum, T. S. Lim, Z. Bin Ahmad, K. A. Mahmood, M. H. Bin Shahid, C. Y. Ang, W. Q. Tan, P. N. Tan, K. S. Yee, W. G. Cheaw, H. S. Boey, A. L. Choo, and B. C. Sew, "A new unmanned aerial vehicle synthetic aperture radar for environmental monitoring," *Progress In Electromagnetics Research*, Vol. 122, 245–268, 2012.

5. Lanari, R., M. Tesauro, E. Sansosti, and G. Fornaro, "Spotlight SAR data focusing based on a two-step processing approach," *IEEE Trans. Geosci. Remote Sens.*, Vol. 39, No. 9, 1993–2004, 2001.

6. Lanari, R., S. Zoffoli, E. Sansosti, G. Fornaro, and S. Serafino, "New approach for hybrid strip-map/spotlight SAR data focusing," *IEE Proc. — Radar Sonar Navig.*, Vol. 148, No. 6, 363–372, 2001.

7. Ding, Z. G., T. Long, T. Zeng, and Y. Zhu, "Deramp range migration processing for space-borne spotlight synthetic aperture radar," *Advances in Space Research*, Vol. 41, 1822–1826, 2008.

8. Lim, S.-H., J.-H. Han, S.-Y. Kim, and N.-H. Myung, "Azimuth beam pattern synthesis for airborne SAR system optimization," *Progress In Electromagnetics Research*, Vol. 106, 295–309, 2010.

9. Wong, F. H. and T. S. Yeo, "New application of nonlinear chirp scaling in SAR data processing," *IEEE Trans. Geosci. Remote Sens.*, Vol. 39, No. 5, 946–953, 2001.

10. Wong, F. H. and I. G. Cumming, "Focusing bistatic SAR data using the nonlinear chirp scaling algorithm," *IEEE Trans. Geosci. Remote Sens.*, Vol. 46, No. 9, 2493–2505, 2008.

11. Yeo, T. S., N. L. Tan, C. B. Zhang, and Y. H. Lu, "A new subaperture approach to high squint SAR processing," *IEEE Trans. Geosci. Remote Sens.*, Vol. 39, No. 5, 954–968, 2001.

12. Chang, Y.-L., C.-Y. Chiang, and K.-S. Chen, "SAR image simulation with application to target recognition," *Progress In Electromagnetics Research*, Vol. 119, 35–57, 2011.

13. Cumming, I. G. and F. H. Wong, *Digital Processing of Synthetic Aperture Radar Data: Algorithms and Implementation*, Artech House, Norwood, MA, 2005.

14. Mao, X., D.-Y. Zhu, L. Wang, and Z.-D. Zhu, "Comparative study of RMA and PFA on their responses to moving target," *Progress In Electromagnetics Research*, Vol. 110, 103–124, 2010.

15. Reigber, A., E. Alivizatos, A. Potsis, and A. Moreira, "Extended wavenumber-domain synthetic aperture radar focusing with integrated motion compensation," *IEE Proc. — Radar Sonar Navig.*, Vol. 153, No. 3, 301–310, 2006.

16. Davidson, G. W., I. G. Cumming, and M. R. Ito, "A chirp scaling approach for processing squint mode SAR," *IEEE Trans. Geosci. Remote Sens.*, Vol. 32, No. 1, 121–133, 1996.

17. Moreira, A., J. Mittermayer, and R. Scheiber, "Extended chirp scaling algorithm for air- and spaceborne SAR data processing in stripmap and scanSAR imaging mode," *IEEE Trans. Geosci. Remote Sens.*, Vol. 34, No. 5, 1123–1135, 1996.